Ore Geology Reviews 91 (2017) 463–476

Contents lists available at ScienceDirect

Ore Geology Reviews

journal homepage: www.elsevier.com/locate/oregeorev

Finite difference modeling of metallogenic processes in the Hutouya Pb-Zn deposit, Qinghai, China: Implications for hydrothermal mineralization

Yanhong Zou[a,b], Yao Liu[a,c,*], Tagen Dai[a,b], Xiancheng Mao[a,b], Yuanbao Lei[d], Jianqing Lai[a,b], Hailong Tian[e]

[a] Computational Geosciences Research Center, Central South University, Changsha 410083, China
[b] Key Laboratory of Metallogenic Prediction of Nonferrous Metals and Geological Environment Monitoring, Ministry of Education, School of Geosciences and Info-Physics, Central South University, Changsha 410083, China
[c] Embedded and Networking Computing Laboratory, Hunan University, Changsha 410082, China
[d] Hunan Institute of Geological Survey, Changsha 410116, China
[e] Key Laboratory of Groundwater Resources and Environment, Ministry of Education, Jilin University, Changchun 130021, China

ARTICLE INFO

Keywords:
FLAC
Qimantage metallogenic belt
Hutouya Pb-Zn deposit
Heat transfer
Hydrothermal mineralization

ABSTRACT

The Hutouya Pb-Zn deposit located in Qinghai, China, is a typical skarn-type polymetallic deposit in the Qimantage metallogenic belt. This belt is characterized by extensive magmatic activity, complicated ore-forming element assemblages and various carbonate-bearing strata. Considering the geological features, mineralogy and geochemistry in the field, we have conducted finite difference simulations of the mineralizing process of galena and sphalerite in terms of a temperature-gradient driven flow. Specifically, we have used modern mineralization theory to quantitatively estimate the duration of the mineralizing process of galena and sphalerite in the Hutouya Pb-Zn deposit. The associated computational simulation results have demonstrated that the hydrothermal fluid flow is a key controlling factor of mineralization in this area. The mineralization of galena and sphalerite corresponds to the quartz sulfide stage, whereas the ore-forming time of galena is later than that of sphalerite. The best metallogenic temperatures of the galena and sphalerite are 150 °C and 250 °C, respectively. These computational results can enhance our understanding of the ore-forming processes in the Hutouya Pb-Zn district.

1. Introduction

The Hutouya Pb-Zn deposit is a typical large-scale, skarn-type, polymetallic ore deposit in the Qimantage area of Qinghai, China (Zhang et al. 2013). Many studies of the ore-formation processes of the Hutouya Pb-Zn deposit have been recently undertaken (He et al., 2014; Shu et al., 2012; Liu et al., 2005; Song et al., 2010). Since hydrothermal mineralization is extremely complex, traditional metallogenic theories of ore-formation have some limitations (Liu and Dai, 2014). Because many factors can affect the formation of mineral deposits, such as pore-fluid flow, temperature distribution, pore pressure variation and physical/chemical properties of surrounding rock, it is very difficult to use traditional metallogenic theories to obtain sufficient details associated with an ore-forming system or the critical geodynamic processes responsible for the formation and localization of orebodies (Liu et al., 2010a; 2010b). Therefore, numerical simulation has emerged as a powerful tool for overcoming the drawbacks associated with traditional metallogenic theories. With significant advancements in computational science and techniques, computational simulation, as a new method for considering the many complex problems in mineral exploration, has attracted increasing research interest. However, the potential influence of thermal or chemical controls on mineralization must be kept in mind when interpreting the results of a numerical model (Potma et al., 2008).

Extensive studies of the ore-forming processes in the upper crust of the Earth have been carried out by Zhao et al. (1998, 2008a, 2008b) and others (Lin et al., 2009; Ord et al., 2010; Yan et al., 2003; Xing and Makinouchi, 2008; Zhao, 2009, 2015, 2016). Many published papers in this field give valuable guidance and methods, which can be briefly classified into the following categories: (1) theoretical study of pore-fluid flow focusing/mixing and convection in fault zones and rocks (Hornby et al., 2006a, 2006b, 2008; Hobbs et al., 2004, 2006, 2007; Schaubs et al., 2016a, 2016b, 2017), (2) theoretical study of chemical dissolution and mineral precipitation instability problems (Hornby et al., 2008; Hobbs et al., 2008, 2010a,b, 2017; Ord et al., 2008a, 2016, 2017; Zhao, 2014; Zhao et al., 2015a, 2015b, 2017; Poulet and Regenauer-Lieb, 2015a, 2015b), (3) application of numerical

* Corresponding author at: Embedded and Networking Computing Laboratory, Hunan University, Changsha 410082, China.
E-mail address: liuyao168@163.com (Y. Liu).

http://dx.doi.org/10.1016/j.oregeorev.2017.09.008
Received 2 November 2016; Received in revised form 4 September 2017; Accepted 11 September 2017
Available online 21 September 2017
0169-1368/

simulation for different ore-forming systems in various geological regions (Zhang et al., 2003, 2008, 2011; McLellan et al., 2004; Gessner et al., 2009; Yang et al., 2010), (4) numerical simulation and theoretical analyses of convective and advective heat transfer in geological systems (Oliver et al., 2006; Ord et al., 2008b; McLellan et al., 2009, 2010; Zhao et al., 2012a, 2013), and (5) numerical simulation of other types of geoscience problems (Alt-Epping and Zhao, 2010; Garven et al., 1993; Lin et al., 2006, 2008; Zhao et al., 2010; Lei et al., 2013; Poulet et al., 2013; Mclellan et al., 2014a, 2014b).

Zhao et al. (2009) have conducted pioneering work on reactive fluid mixing and mineralization in pore-fluid saturated hydrothermal systems. Specifically, the mineralization rate concept and modern mineralization theory (Phillips, 1991; Zhao et al., 2002, 2008a) were successfully applied to finite element simulation of mineralization patterns in hydrothermal systems and excellent results have been obtained (Hobbs et al., 2000, 2006; Reid et al., 2012a, 2012b). In this paper, the function of Zhao's modern mineralization theory (Zhao et al., 2002, 2008a) is incorporated into the FLAC2D (Fast Lagrangian Analysis of Continua in Two Dimensions) code via the FISH language, which is a programming language embedded in FLAC2D that enables the user to define new variables and functions. Consequently, we can apply this theory to predict the mineralization patterns in the Hutouya Pb-Zn deposit.

The Hutouya Pb-Zn deposit contains high-grade Pb-Zn ore on a large scale (Zhang et al., 2013). Due to economic efforts to develop western China, the Hutouya Pb-Zn deposit has been studied extensively by many researchers (Gao et al., 2013; Yang et al., 2015). These studies are useful for understanding the ore-formation of the Hutouya Pb-Zn deposit, but the exact metallogenic temperature of the Pb-Zn ore in this region is still unknown. Some researchers (Liu et al., 1984) believe that the mineralization temperature of the Pb-Zn ore in the Hutouya ore district may be greater than 300 °C, but other studies (Lu, 1975; Lei, 2014) indicate that the mineralization temperature of the galena and sphalerite in the Hutouya ore district is in the range of 148–262 °C. New studies (Xu, 2010; Lei, 2014) have shown that the mineralization temperature range of the galena and sphalerite in the Hutouya ore district should be approximately 220–303 °C, with an average of 241 °C. The galena and sphalerite in the Hutouya Pb-Zn deposit have the typical characteristics of a magmatic hydrothermal deposit. We can briefly summarize the previous research (Liu et al., 2006; Xu, 2010) as follows: (1) the storage situation and distribution characteristics of the galena and sphalerite resources in the Hutouya Pb-Zn deposit have been investigated; (2) the strata and structure in the Hutouya ore district have been determined; and (3) the Hutouya Pb-Zn polymetallic deposits are mainly epithermal to mesothermal deposits. In addition, new research (Li and Xi, 2012; Gao et al., 2015; Lei et al., 2014a; Ma et al., 2013; Zhao et al., 2014) has also contributed valuable insights that can be summarized as follows: (1) the metallogenetic material arises from hydrothermal fluids that contain Pb and Zn ions; (2) the hydrothermal solution moves upward along the fractures; and (3) the common ore-forming process is dominated by the penetration of hydrothermal fluids through the carbonate layer, where chemical reaction should have occurred easily.

However, the ore-forming process in the Hutouya Pb-Zn deposit is very complicated. Several key factors have still been ignored. For example, (1) the effects of temperature and pressure gradients on the galena and sphalerite ore deposits have not been analyzed; (2) although the control of structures for the localization of the orebodies is emphasized, the migration of the mineralization elements has rarely been considered; (3) research on associated chemical reactions that precipitate galena and sphalerite is still limited; (4) many studies have been based on the traditional methods, and the new computational simulation approach has not been applied in the Hutouya Pb-Zn deposit; and (5) the chemical factor of the galena and sphalerite ore has seldom been analyzed. Therefore, it is necessary to develop innovative knowledge models for understanding ore-forming processes in detail to facilitate the understanding of ore-formation processes in the Hutouya Pb-Zn deposit.

In this study, we use the numerical simulation method used by Liu and Dai (2015) and the modern mineralization theory of Zhao et al. (2002) to investigate the ore-forming mechanism of the Hutouya Pb-Zn deposit. The outcome of this study contributes to the emerging computational geoscience discipline, whose methodology has been extensively used to solve many different types of geoscience problems (Walshe et al., 2001; Schmidt Mumm et al., 2010; Hobbs et al., 2011; Ord et al., 2012, 2013a,b; Peng et al., 2008, 2011). The metallogenic temperature and ore-forming process in the Hutouya Pb-Zn deposit were investigated using the FLAC2D numerical simulation method in the present study. This new method for investigating galena and sphalerite mineralization helps to provide a better understanding of ore-formation and mineralization in the Hutouya Pb-Zn deposit, although previous research (Lei, 2014) still provides some useful information.

2. Establishment of a geological/conceptual model for the Hutouya Pb-Zn deposit

Existing extensive studies (Zhao et al., 2008b; 2009) have indicated that when using the computational geoscience methodology, the following three kinds of models need to be established for a typical mineralization problem: a geological/conceptual model, a mathematical model and a computational simulation model (Zhao et al., 2009). In this section, we address the key issues associated with establishing a geological/conceptual model for the Hutouya Pb-Zn deposit, which requires answers to five questions (Gow et al., 2002; Hobbs et al., 2000; Ord et al., 2002; Schaubs and Zhao, 2002; Sorjonen-Ward and Zhang, 2002; Zhao et al., 2012b): (1) What are the geometry and material distribution characteristics of the entire mineralizing system? (2) What is the geological history of the system, especially the timing, pressure and temperature history? (3) What processes were responsible for driving the fluid flow? (4) What were the physical and chemical processes involved with and the signatures of the fluids responsible for mineralization? (5) What were the processes involved in the mineral precipitation and development and changes at the mineralization site? To answer these questions, we must understand the regional geology, deposit characteristics and metallogenic model.

2.1. Geological characteristics of the Hutouya Pb-Zn deposit

The Qimantage region in Qinghai province is located in the southwest margin of the Qaidam Basin in the northeast of Qinghai-Tibet Plateau and lies in the Qaidam block along the East Kunlun orogenic belt, which is an important polymetallic metallogenic belt (Li and Xi, 2012).

From the oldest to the youngest, the strata in this area are the Baishahe Formation of Jinshan Group of Paleoproterozoic to Mesoproterozoic age, the Xiaomiao Formation of Changcheng system, the Langyashan Formation of the Jixianian system, the Tanjianshan Formation of the Ordovician-Silurian age, the Maoniushan Formation of Devonian age, the Dagangou and Di'aoshu Formations of Carboniferous age, and the Elashan Formation of Triassic age, the Lulehe Formation of Paleogene age, the Youshashan Formation of Neogene age and the Hongji Formation of Quaternary age (Table 1) (Shu et al., 2012). Except for plutonic rocks in the Baishahe Formation and continental pyroclastic rocks and lavas in the Elashan Formation, carbonate rocks are present in all strata, and especially developed in the Dagangou and Di'aoshu Formations

The tectonic activities in the region were mainly dominated by the NW-trending fault structure and the nearly E-W trending secondary fault structure as well as the short axis and septal folds (Fig. 1). Of these, the NW-trending fault structure has controlled the magmatic activities in this area, and the secondary fault structures have controlled

Table 1
Stratigraphy and thickness of the strata in the Qimantage area (see Luo, 2014; Zhang et al., 2013; Yao et al., 2015).

Period	Epoch	Series	Lithostratigraphic Unit	Stratum Code	Lithology description	Strata Depth
Cenozoic	Quaternary		Hongji Formation	Q	Deluvium	10–30 m
	Neogene	Pliocene	Youshashan Formation	N_4y	Conglomerate	12–26 m
			Shizigou Formation	N_2s	Sandstone	3–8 m
		Miocene	Ganchaigou Formation	N_1g	Limestone	8–16 m
	Paleogene		Lulehe Formation	E_1l	Quartz Sandstone	4–9 m
Mesozoic	Cretaceous	Early	Quanyagou Formation	K_1q	Conglomerate	33–52 m
	Jurassic	Late	Caishiling Formation	J_3c	Sandstone	45–69 m
		Early	Dameigou Formation	J_1d	Coal-bearing Clastic rocks	26–51 m
	Triassic	Late	Elashan Formation	T_3e	Pyroclastic Rocks	87–136 m
Palaeozoic	Permian	Early	Dachaigou Formation	P_1d	Limestone	45–60 m
	the Carboniferous	Late	Di'aoshu Formation	C_2d	Dolomite	132–165 m
		Early	Dagangou Formation	C_1dg	Limestone	50–58 m
			Shiguaizi Formation	C_1s	Siliceous Limestone	20–45 m
	Devonian	Late	Maoniushan Formation	D_3m	Dolomite	50–86 m
	Ordovician	Late	Tanjianshan Formation	O_3t	Volcanic rock	46–92 m
Proterozoic	Neoproterozoic	Jx	Langyashan Formation	Jxl	Dolomite	98–156 m
	Mesoproterozoic	Ch	Xiaomiao Formation	Chx	Siliceous rocks	> 300 m
	Paleoproterozoic		Baishaheyan Formation	Pt_1b	Hornblende	> 200 m

the mineralization (Ma et al., 2012; Lei et al., 2014a). The strong magmatic activities were developed from Jinningian to Yanshanian and were dominated by Hercynian-Indosinian magmatism, including mafic and intermediate-acid, intrusive and extrusive rocks (Fig. 1). The magmatic activities were closely associated with the mineralization of porphyry and skarn deposits in this area and provided material basis and energy for mineralization (Lai et al., 2015).

Fig. 2 shows the Hutouya Pb-Zn district outcrop of the Langyashan Formation of the middle Proterozoic Jixianian Period, the Ordovician-Silurian Tanjianshan Group, the Early Carboniferous Dagangou Formation, the Late Carboniferous Di'aoshu Formation, the Triassic Elashan Formation and the Quaternary. The Langyashan Formation is predominantly marble and limestone. The lithology of the Ordovician-Silurian Tanjianshan Group consists mainly of carbonate-bearing basalt, tuff and siliceous rocks, with marble and grey-black bioclastic limestone in the Dagangou Formation of lower Carboniferous. The Di'aosu Formation of upper Carboniferous is mainly formed by marble with interbedded grey-black bioclastic crystalline limestone, while the Triassic Elashan Formation is mainly crystal tuff containing quartz and K-feldspar crystal. The dip of each stratum is steep, approximately 45–70 °. The Quaternary covers the valley of each mountain with an apparent irregular distribution.

There are three principal structures in this area that have a nearly NW-trending inter-layer slippage fracture (Fig. 2). The skarn is apparently visible in the inter-layer slippage fracture and determines the occurrence of the No. IV, VI and VII ore zones.

The magmatic rocks in this area are complex, ranging from basic to acid exposed rocks. The intrusive rocks, which intruded the Dagangou and Di'aoshu Formations in the Middle-Late Indosinian, include mainly K-feldspar granite, monzonitic granite and granodiorite (Fig. 2). The skarn was formed around these magmatic rocks; in addition, veins of diorite, diorite porphyry and diabase developed. Several studies have shown that the nearly E-W trending secondary fault structure formed prior to mineralization (Lei, 2013; Lai et al., 2015), so deformation was not involved in the ore-forming process.

A total of nine ore zones are currently exposed in this area, and they are far apart from each other (Zhang et al., 2013). Based on the recoverable resources, the No. VII ore zone is the most important, and its orebody has a layer-like shape, and visibly penetrates several strata. The orebody mainly includes Pb, Zn and Cu polymetallic ore, which has an E-W trend with length of approximately 0.5–2 km. The No. VI ore zone is considered to have secondary importance, and the third most important is the No. II ore zone (Fig. 2). Sphalerite and chalcopyrite are the dominant metallic minerals in the No. VI, VIII and IX ore zones. In the No. II ore zone, the ore-forming metals are mainly composed of magnetite, chalcopyrite and stannite. In the No. I and III ore zones, the minerals are primarily composed of magnetite (Fig. 2). These ore zones, unlike the No. VII ore zone, are irregularly shaped, striped and lenticular, and they occupy the contact zone between the K-feldspar granite, monzonitic granite and carbonate or the fault zone associated with skarn. The major mineral species in the skarn-type orebodies comprise Pb-Zn ore, Fe and Cu. The primary ore minerals are sphalerite, galena, magnetite, chalcopyrite and porphyry copper, followed by arsenopyrite and molybdenite and small amounts of chalcocite, pyrrhotite and pyrite. The vein minerals are mainly calcite, garnet and epidote and small amounts of diopside, fluorite and quartz. The skarn-type ore belt and the northern IV ore belt are associated with strong wall rock alteration and both ore belts have intense skarn, silicification and carbonatization. Mineralization can be classified into four stages: depositional metallogenesis, skarn formation, quartz sulfide and surface oxidation. Sphalerite and galena were formed in the Pb-Zn sulfide phase of the quartz sulfide stage, and the galena was formed later than the sphalerite (Lei et al., 2014b).

2.2. Metallogenic model for the Hutouya Pb-Zn deposit

The Qimantage area was in a post-collision orogenic stretch environment during the Middle-Late Indosinian Period. The granitic magma, which was formed by granite re-melting along the subduction zone, intruded upwards into the carbonate strata of the Di'aosu Formation (Lei, 2013), while the monzonitic granite and K-feldspar granite formed. When the magma invaded, the diagenetic minerals gradually crystallized and consolidated, the high temperature magma gas-liquid fluid that was enriched in volatile components was forced out, and the metasomatism occurred around the contact between the granitic and carbonate rocks (Fig. 3). Consequently, skarn was formed and high-temperature mineralization elements such as Fe, W, and Sn, were enriched. Some of the magma fluid migrated along the faults, and metasomatism occurred around the faults. The irregular layer-like shape of Pb-Zn orebodies subsequently formed along the fault zone and the inter-layer fracture zones in the Di'aosu and Langyashan Formations. Most of the ore-forming material came from the magmatic rock, such as Pb, Zn, Cu, S and Fe, with small amount from the strata during the metasomatic process between the magmatic gas-fluid flow and the

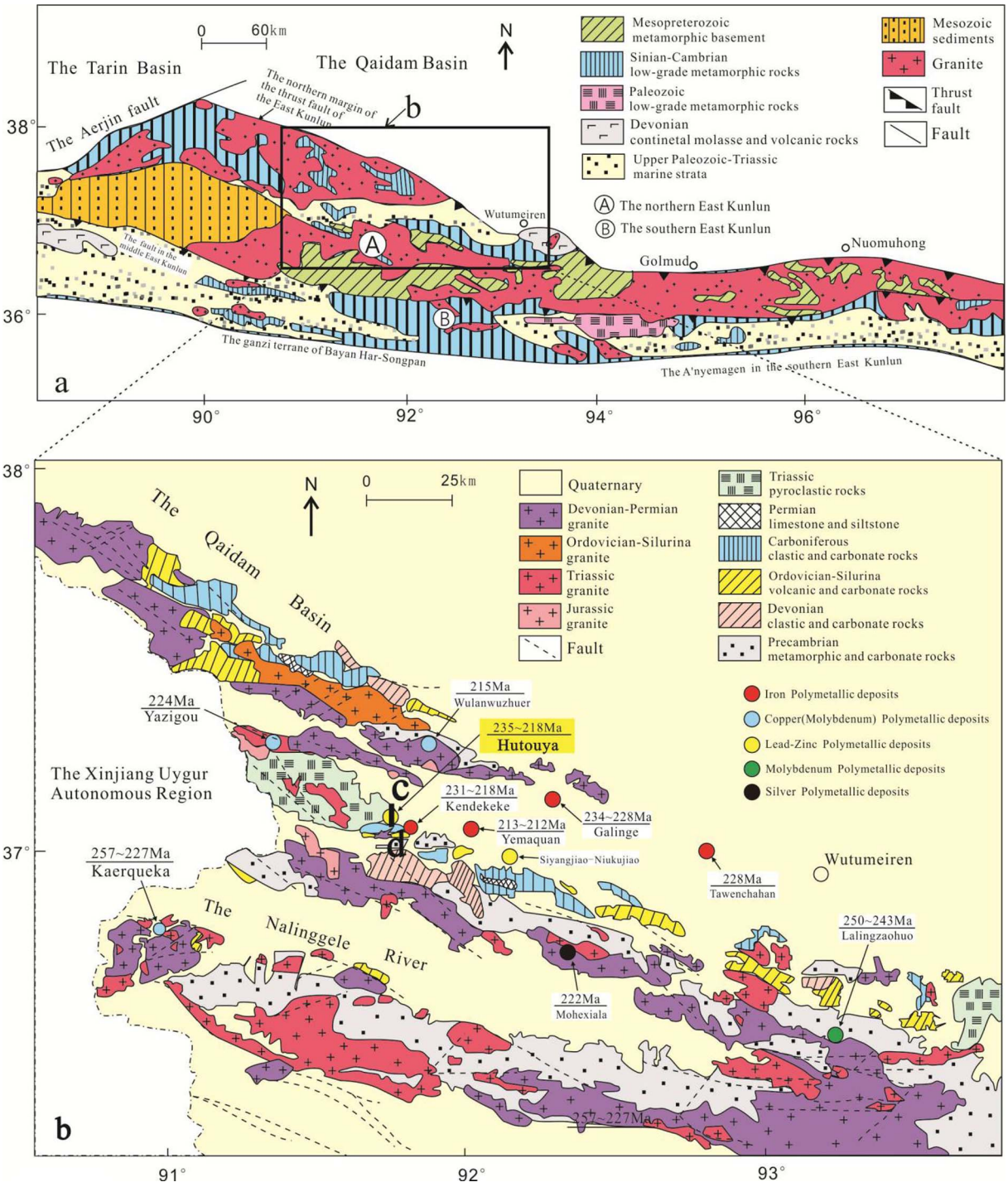

Fig. 1. Geological map of the polymetallic deposits in the part of the Qimantage area, showing the location of the Hutouya Pb-Zn deposit: (a) entire view; and (b) zoomed-in view (Yao et al., 2015).

strata. However, the energy required for metallogenisis was mainly produced by the magmatic rocks. From the early to the late mineralization period, the salinity and temperature of the ore-forming fluid gradually decreased, with magmatic gas-liquid fluids predominating during the early period and joined by low-temperature and low-salinity fluids during the late period (Lei, 2013).

2.3. Geological/conceptual models for the Hutouya Pb-Zn deposit

Based on the geological and metallogenic model discussed in the previous section, we consider only the top-right corner of Fig. 3 as the metallogenic area of the Hutouya Pb-Zn polymetallic deposit. We constructed a generic model and a realistic computational model to simulate the thermal flow-driven mineralization processes associated with the Hutouya Pb-Zn polymetallic deposit. Fig. 4 shows the generic 2D model for the Hutouya Pb-Zn deposit. This model is constructed on the basis of the cross section along line cd in Fig. 1. Some assumptions are made to reflect the subsurface geological conditions of the Hutouya Pb-Zn deposit and other features that are relevant to pore-fluid flow in the Hutouya ore district. As shown in Table 1, previous studies (Luo, 2014; Qu et al., 2015; Zhang et al., 2013) indicated that the deepest level of the exploration line is nearly 500 m. The specific distance can

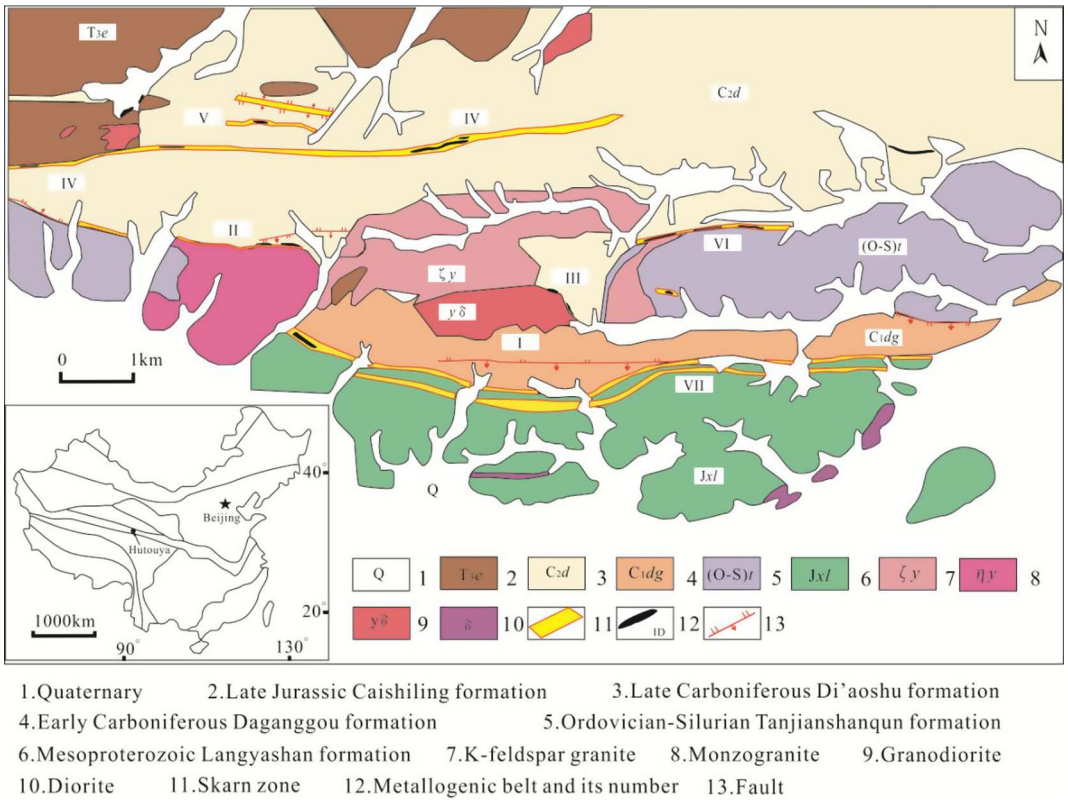

Fig. 2. Geological sketch map of the Hutouya Pb-Zn polymetallic ore district (Zhang et al., 2013).

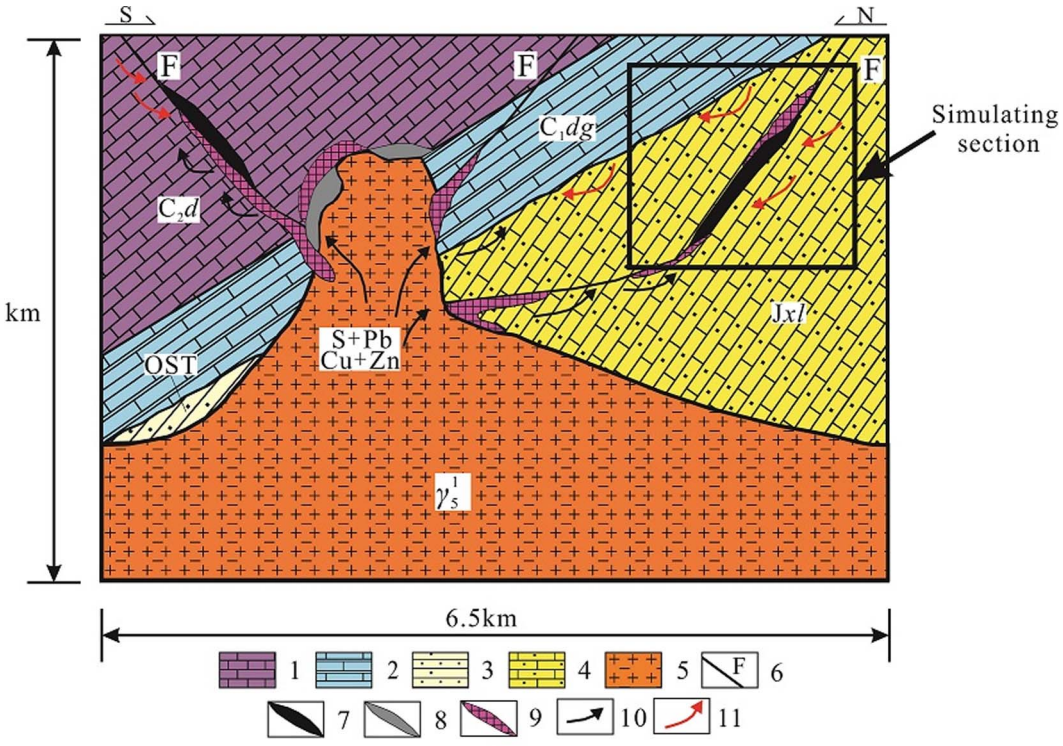

1. Di'aoshu formation of the Late Carboniferous 2. Dagangou formation of the Early Carboniferous
3. Ordovician-Silurian Tanjian hill group 4. Langya formation of the Jixian period
5. Middle-Late Indosinian granite intrusion (include K-feldspar granite and granodiorite)
6. EW trend ore-controlling fracture 7. Lead-zinc ore body 8. Iron polymetallic ore body
9. Skarn zone 10. Direction of ore-bearing fluid flow with high temperature and high salinity
11. Direction of fluid flow in the formation with low temperature and low salinity

Fig. 3. Metallogenic model of the Hutouya Pb-Zn polymetallic deposit (Lei, 2013).

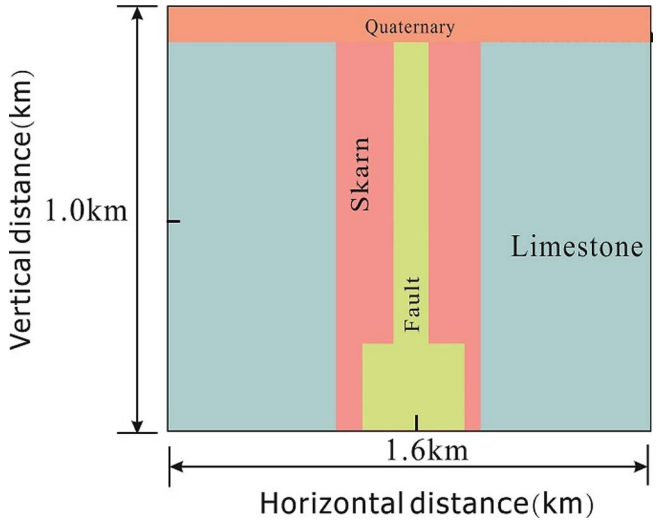

Fig. 4. The generic model of the Hutouya Pb-Zn deposit.

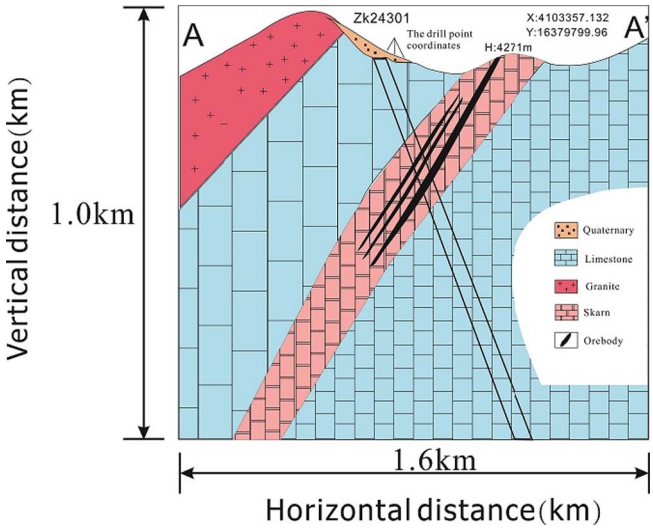

Fig. 5. The geological section along A-A′ exploration line in the Hutouya Pb-Zn deposit.

be calculated by the depth of the exploration line considering the distance of the pore-fluid flow and its mobility, so an extended model was constructed and filled with the corresponding rock. This implies that the depth of the model should be greater than 500 m. The simulation region in the present study is shown in Fig. 3. The shape and scale of the simulation region and previous studies (Lei, 2013; Lei et al., 2014a) indicate that a FLAC2D model with a 1.6-km-long and 1-km-deep cross-section would be reasonable. The horizontal dimension of the model is 1.6 km, which is similar to the length of line cd in Fig. 1. We assume the initial hot pore-fluid in the fault zone was 400 °C at the base, and a previous study (Lei, 2014) showed that the ore-forming temperature of the galena and sphalerite was approximately 148-262 °C, but another study (Xu, 2010) showed that the ore-forming temperature ranged between 220 °C and 303 °C. The temperature of the intruding magma must exceed the ore-forming temperature (Liu et al., 2011; Liu and Dai, 2014). As mentioned previously, the mineralization temperature of the galena and sphalerite are not precisely known. Since the Hutouya Pb-Zn polymetallic deposits are mainly epithermal to mesothermal deposits (Zhang et al., 2013), the highest temperature used for the TOUGHREACT calculation in the experimental data of the equilibrium concentration of the Pb^{2+} and Zn^{2+} are approximately 350 °C. The equilibrium concentration of Pb^{2+} and Zn^{2+} at temperatures between 350 °C and 400 °C were extrapolated. Thus, 400 °C is an acceptable initial intrusion temperature for the numerical simulations. As previously mentioned, the nearly E-W trending secondary fault structure was formed before mineralization, and deformation was not involved in the ore-forming process (Lei, 2013; Lai et al., 2015). When the intrusion initiated at the bottom of the fault, the temperature difference provided the driving force for pore-fluid flow, so we believe that the driving force of pore-fluid flow was the temperature gradient. Since the depth of the model is assumed to be 1 km, the pressure calculation indicates that lithostatic pressure at the bottom of the model was almost 25 Mpa, but it was approximately 10 Mpa at the upper part of the model, where the mineralization of Pb and Zn occurred (Lei, 2013). Therefore, we chose 10 Mpa as the input pore-fluid pressure in the TOUGHREACT calculation.

The 2D generic model consists of 4800 four-node grid cells. The available geological data (Ma et al., 2013) indicate that many orebodies are located along the contact zone between the magmatic intrusion and the carbonate layer. Fig. 4 shows that the main wall-rock types are composed of limestone, skarn, quaternary and fault. The depth of the fault zone is assumed to approximate the perpendicular distance. The exposure of many orebodies on the surface (Gao et al., 2013) implies that the fault may extend to the surface, so the depth of the fault zone was determined based on this assumption.

The numerical model in the second example was constructed by considering geological section maps of the Hutouya Pb-Zn deposit, as shown in Fig. 6. This realistic model, which is also called the geological conceptual model (Fig. 5), comprises 19,200 four-node grid cells. The rocks considered in this model are limestone, quaternary, skarn, fault zone and granite. One fault zone, with dip angles of 65° to the east is present. The fault distribution in the model is based on the geological cross-section map in Fig. 1 and the metallogenic model in Fig. 3. Considering rock erosion during mineralization as well as fluid mobility, the extended model was established and filled with the corresponding rock.

3. Establishment of a mathematical model for the Hutouya Pb-Zn deposit

3.1. Brief introduction to FLAC software

The FLAC2D code (Itasca Consulting Group, 2012) was used to simulate the mineralization process of the Hutouya Pb-Zn deposit. FLAC2D is a two-dimensional explicit finite difference code that has been widely used for solving complex geoscience problems (Liu et al., 2011; McLellan et al., 2010; Oliver et al., 2006).

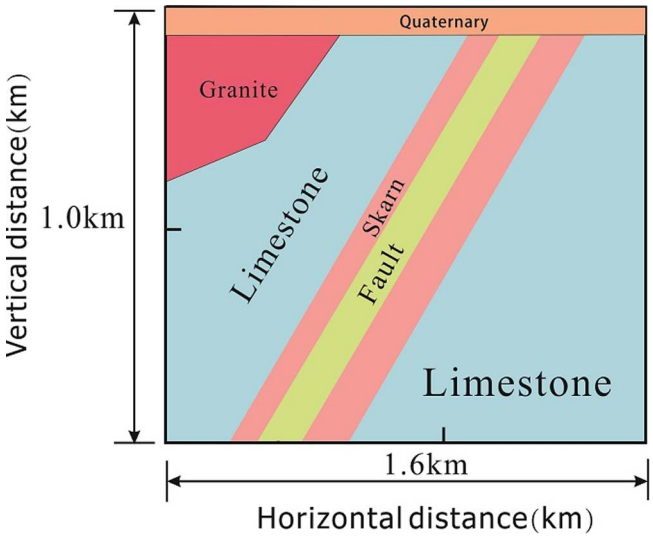

Fig. 6. The geological conceptual model of the Hutouya Pb-Zn deposit.

Compared with finite element models, explicit finite difference models have the following advantages: (1) they can be used to calculate nonlinear constitutive relationships directly, without excessive memory requirements; (2) a large number of grid cells may be modeled with a modest memory requirement because there is no global stiffness matrix that must be inverted during each time-step; and (3) FLAC2D is robust in the sense that it can handle any constitutive model with no adjustment to the solution algorithms and techniques for different constitutive models. The open programming design option makes it easy for a user to use their own programming techniques in the framework of the FLAC2D code via the FISH language. Large-scale complex problems can be simulated using the FLAC2D code, and the computational time does not increase significantly for highly nonlinear problems (Cundall and Board, 1988; Xiao et al., 2005; Tiziana et al., 2013).

3.2. Governing mathematical equations associated with the mathematical model for the Hutouya Pb-Zn deposit

The hydrothermal transformation of galena and sphalerite ore is assumed to be caused by thermal process controlled by temperature gradient in porous rocks (Zhao et al., 2008a; 2009). As hydrothermal fluid passed through the carbonate layer, a strong chemical reaction of contact metasomatism between carbonate and ore-bearing hydrothermal solution occurred, forming galena and sphalerite ores in the Hutouya Pb-Zn deposit. The mineralization rate (Phillips, 1991; Zhao et al., 2002; Ord et al., 2002) has been successfully used to simulate siderite precipitation in the Caiyuanzi ore deposit (Liu and Dai, 2015) and can be further extended to explain the nonferrous metal ore-forming process, by which hydrothermal transformation formed both galena and sphalerite ores in the Hutouya Pb-Zn deposit. The governing equations used for simulating the galena and sphalerite ore-forming process in the Hutouya Pb-Zn deposit in the FLAC2D models can be briefly described as follows:

$$\upsilon_x^f = -\frac{k_x \lambda(s)}{\mu}\frac{\partial P}{\partial x} \tag{1}$$

$$\upsilon_y^f = -\frac{k_y \lambda(s)}{\mu}\left(\frac{\partial P}{\partial y} - \rho_f g\right) \tag{2}$$

$$q_x^T = -(\phi\xi^f + (1-\phi)\xi^s)\frac{\partial T}{\partial x} \tag{3}$$

$$q_y^T = -(\phi\xi^f + (1-\phi)\xi^s)\frac{\partial T}{\partial y} \tag{4}$$

$$\rho_f = \rho_0[1-\beta(T-T_0)] \tag{5}$$

where υ_x^f and υ_y^f are Darcy velocities of fluid flow in x and y directions, respectively; P is pressure of pore-fluid; k_x and k_y are mobility coefficients (FLAC's permeability) in x and y directions, respectively; $\lambda(s)$ is a function of saturation s; μ is dynamic viscosity of pore-fluid; g is the component of gravitational acceleration in y direction; ρ_f is density of pore-fluid; q_x^T and q_y^T are thermal fluxes in x and y directions, respectively; ξ^f and ξ^s are thermal conductivity coefficients of pore-fluid and solid matrix, respectively; T is temperature; and ϕ is porosity; ρ_0 is reference density of pore-fluid; β is volumetric thermal expansion coefficient; and T and T_0 are the temperature and reference temperature of the pore-fluid and surrounding medium, respectively.

Eqs. (1) and (2) are Darcy's law for describing pore-fluid flow in x and y directions, respectively. Eqs. (3) and (4) are Fourier's law for describing heat transfer in x and y directions, respectively, and Eq. (5) is the relationship between temperature and pore-fluid density. These governing equations describe the conservation of mass, energy and momentum. The coupled thermal-hydrological constitutive relationships can be found in the literature (Zhao et al., 2009; Lin et al., 2003; Liu et al., 2010a).

3.3. The concept of mineralization rate

The mineralization rate of a mineral is defined as the variation in the mineral weight per unit volume of rock per unit time during mineralization (Zhao et al., 2002). Using this definition, a positive mineralization rate of Pb-Zn ore indicates that galena and sphalerite are in solution in a hydrothermal system, whereas a negative mineralization rate means that galena and sphalerite have precipitated in a hydrothermal system (Zhao et al., 2002, 2008a). The mathematical formula of mineralization rate can be deduced from the mass conservation law as follows (Zhao et al., 2002, 2008a):

$$u_j C_{k,j}^e = (D_{ij}^e C_{k,j}^e) + \phi R_k \quad (k = 1,2,...,M) \tag{6}$$

where u_j is the velocity component in x_j direction; C_k^e is the equilibrium concentration of a mineral k , R_k is a source/sink term, M is total number of minerals considered in the ore-forming system, ϕ is porosity of the porous rock, and D_{ij}^e is the second-order diffusivity tensor of the porous rock. For mineralization problems, the diffusion term on the right-hand side of Eq. (9) is usually much smaller than the advection term. Thus, Eq. (6) can be approximately expressed as

$$MR_k = u_j C_{k,j}^e = \phi R_k \tag{7}$$

where MR_k is the mineralization rate of a mineral k.

In general, the equilibrium concentration of a mineral is a function of temperature, pressure and other relevant minerals as follows:

$$C_k^e = f(T,P,C_1,C_2,...,C_N) \tag{8}$$

where T is temperature; P is pore-fluid pressure; C_k^e is the equilibrium concentration of a mineral k ; C_r ($r=1, 2, \ldots, N$) is the concentration of a mineral r; and N is number of relevant minerals/species necessary to determine the equilibrium concentration of a mineral/species k in a chemical reaction. According to the chain rule, substituting Eq. (8) into Eq. (7) yields the following equation (Zhao et al., 2002, 2008a):

$$MR_k = \frac{\partial C_k^e}{\partial T}(u_j T_{,j}) + \frac{\partial C_k^e}{\partial T}(u_j P_{,j}) + \sum_{r=1}^{n}\frac{\partial C_k^e}{\partial C_r}(u_j C_{r,j}) \tag{9}$$

3.4. Equilibrium concentrations of Pb^{2+} and Zn^{2+}

Previous studies (Luo, 2014; Ma et al., 2012) indicate that galena and sphalerite in the Hutouya ore district are associated with the Mesoproterozoic Langyashan Formation, the Early Carboniferous Di'aoshu Formation and the Late Ordovician Tanjianshan Formation. Previous research (Li et al., 2003) has also shown that the Hutouya Pb-Zn polymetallic deposit is a magmatic hydrothermal deposit. The ore-bearing hydrothermal fluid is rich in sodium and chloride ions, and the migration forms of galena and sphalerite in the ore-bearing hydrothermal fluid are most likely $PbCl^+$, $ZnCl^+$, $PbHS^+$ and $PbHS^+$. Because the temperature of ore-bearing hydrothermal fluid progressively decreases, the ore-forming elements precipitate.

For the mixing of reactive sulfide fluids, the corresponding chemical formula can be expressed, in ionic form:

$$PbCl^+ + ZnCl^+ + Ca^{2+} + CO_3^{2-} + 2HS^- \overset{w}{\Leftrightarrow} PbS\downarrow + ZnS\downarrow + CaCl_2 + H_2O + CO_2\uparrow \tag{10}$$

$$PbHS^+ + ZnHS^+ + CO_3^{2-} \overset{w}{\Leftrightarrow} PbS\downarrow + ZnS\downarrow + H_2O + CO_2\uparrow \tag{11}$$

where w is the overall reaction rate constant, which is strongly dependent on temperature, from the thermodynamic point of view.A previous study (Zhang et al., 2013) showed that galena and sphalerite ore could be easily precipitated when the solution pH is 7. Because the pH of the $NaCl$ aqueous solution is approximately 7, it can be used as a buffer for galena and sphalerite mineralization. Since the equilibrium concentrations of Pb^{2+} in galena and Zn^{2+} in sphalerite were directly calculated by the TOUGHREACT code (Xu et al., 2004) between 25 and

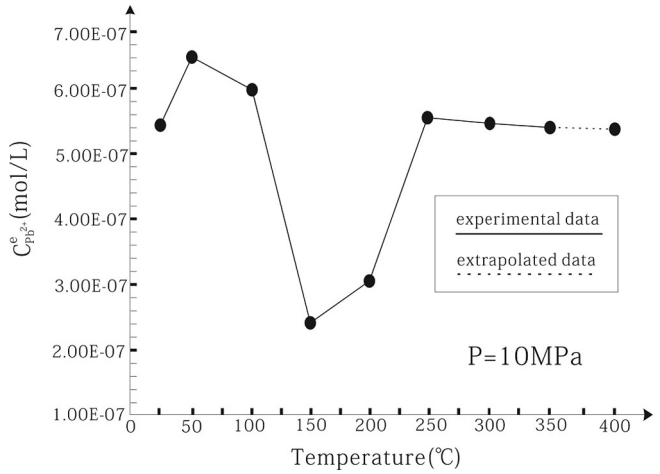

Fig. 7. Variations of Pb^{2+} equilibrium concentration with temperature (in the NaCl buffer). The experimental data are provided by the TOUGHREACT code (Xu et al., 2004).

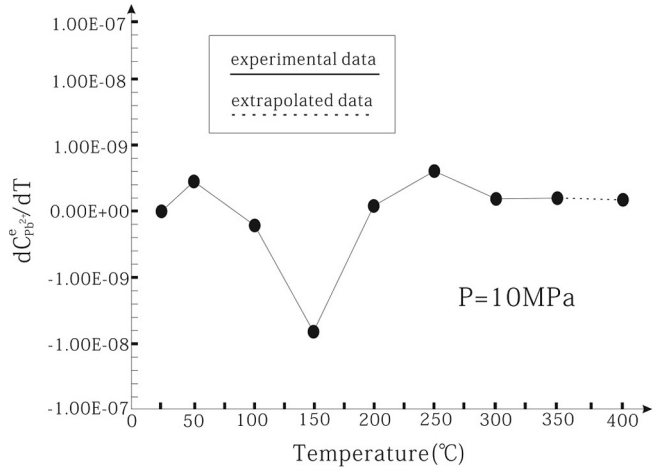

Fig. 8. Variations of the differentiation of Pb^{2+} equilibrium concentration with temperature (in the NaCl buffer). The experimental data are provided by the TOUGHREACT code (Xu et al., 2004).

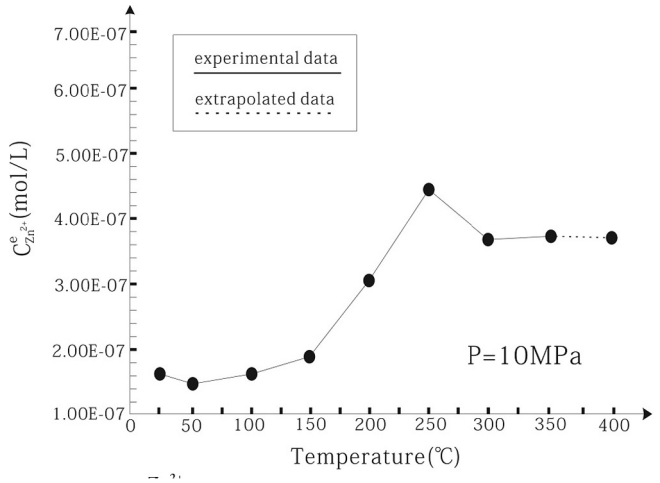

Fig. 9. Variations of Zn^{2+} equilibrium concentration with temperature (in the NaCl buffer). The experimental data are provided by the TOUGHREACT code (Xu et al., 2004).

400 °C in *NaCl* solution that comprises silicon oxide, calcium carbonate, magnesium carbonate and sodium chloride, it can be used in this study to determine the precipitation pattern of galena and sphalerite. For a *NaCl* buffer, the equilibrium concentration of Pb^{2+} in galena between

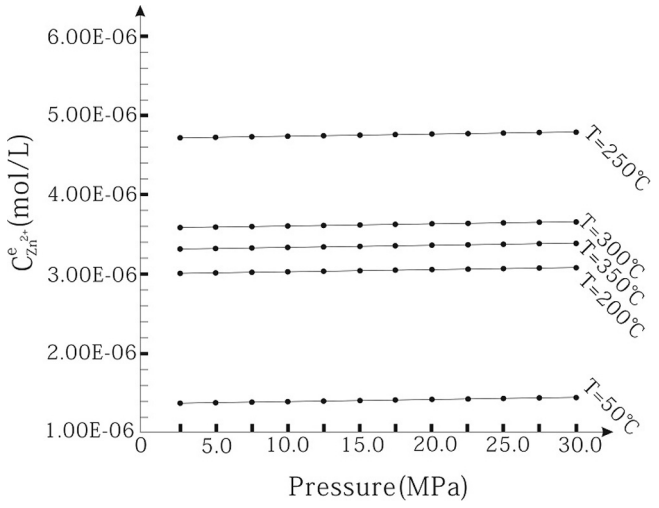

Fig. 10. Variations of Zn^{2+} equilibrium concentration with pressure (in the NaCl buffer). The experimental data are provided by the TOUGHREACT code (Xu et al., 2004).

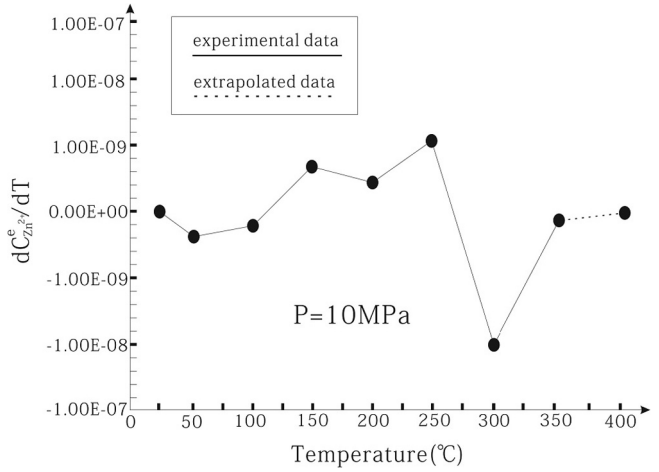

Fig. 11. Variations of the differentiation of Zn^{2+} equilibrium concentration with temperature (in the NaCl buffer). The experimental data are provided by the TOUGHREACT code (Xu et al., 2004).

25 and 400 °C can be expressed in a stepwise manner as

$$\begin{aligned}
\log C^e_{Pb^{2+}} &= 0.002854T - 6.2518 \ (25\ ^\circ\text{C} \leqslant T < 50\ ^\circ\text{C}) \\
\log C^e_{Pb^{2+}} &= -0.000974T - 6.1805 \ (50\ ^\circ\text{C} \leqslant T < 100\ ^\circ\text{C}) \\
\log C^e_{Pb^{2+}} &= -0.008569T - 6.2291 \ (100\ ^\circ\text{C} \leqslant T < 150\ ^\circ\text{C}) \\
\log C^e_{Pb^{2+}} &= 0.002694T - 6.6576 \ (150\ ^\circ\text{C} \leqslant T < 200\ ^\circ\text{C}) \\
\log C^e_{Pb^{2+}} &= 0.005421T - 6.5229 \ (200\ ^\circ\text{C} \leqslant T < 250\ ^\circ\text{C}) \\
\log C^e_{Pb^{2+}} &= -0.000315T - 6.2518 \ (250\ ^\circ\text{C} \leqslant T < 300\ ^\circ\text{C}) \\
\log C^e_{Pb^{2+}} &= -0.000328T - 6.2676 \ (300\ ^\circ\text{C} \leqslant T < 350\ ^\circ\text{C}) \\
\log C^e_{Pb^{2+}} &= -0.00034T - 6.284 \ (350\ ^\circ\text{C} \leqslant T < 400\ ^\circ\text{C})
\end{aligned} \tag{12}$$

where $C^e_{Pb^{2+}}$ is the equilibrium concentration of Pb^{2+} . Note that the equilibrium concentration of Pb^{2+} at temperatures between 350 and 400 °C is extrapolated.Fig. 7 shows the behavior of Pb^{2+} equilibrium concentration with temperature in the *NaCl* buffer, and Fig. 8 shows the behavior of the derivative of Pb^{2+} equilibrium concentration with temperature in the *NaCl* buffer. The solid line is experimental data, and the dotted line is extrapolated.Similarly, the equilibrium concentration of Zn^{2+} in sphalerite between 25 and 400 °C can be expressed in a stepwise manner as

Table 2
Rock material parameters assigned for the generic model. The data are obtained from previous studies (Cai et al., 2002; Liu and Dai, 2014, 2015; Ju et al., 2011).

Rock types	Density (kg/m^3)	Specific heat capacity (J/kg·K)	Linear thermal expansion coefficient (10^{-6}/K)	Conductivity (W/m·K)	Fluid volumetric thermal expansion (10^{-6}/K)	Grain volumetric thermal expansion (10^{-6}/K)	Permeability (m^2)	Porosity (%)
Limestone	2460	660	6.60	3.2	620	28.1	1.00×10^{-14}	20
Quaternary	2580	790	8.40	3.4	720	31.9	2.00×10^{-12}	25
Skarn	2480	730	9.60	3.2	640	29.6	2.00×10^{-14}	20
Fault zone	2400	2200	13.90	3.0	820	41.7	1.00×10^{-10}	30

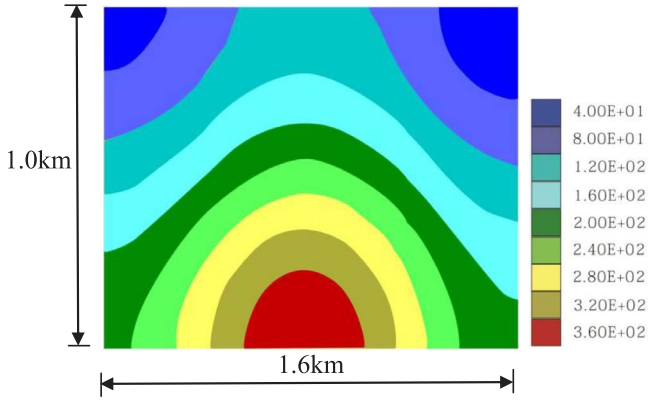

(a) Temperature distribution (℃)

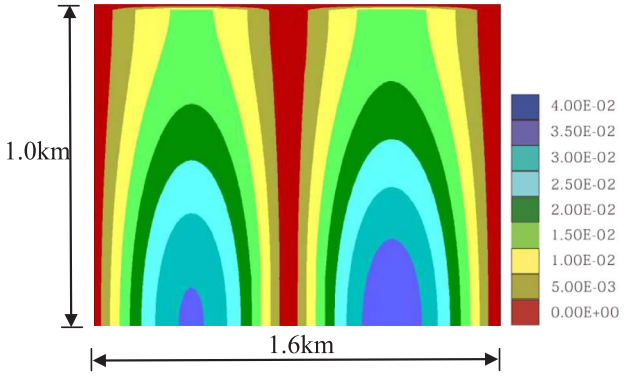

(b) The temperature gradient in the *x* direction (℃/m)

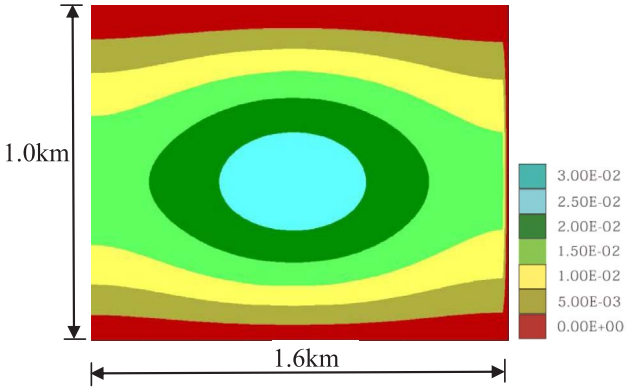

(c) The temperature gradient in *y* direction (℃/m)

Fig. 12. Distributions of (a) temperature, (b) temperature gradient in *x* direction and (c) temperature gradient in *y* direction.

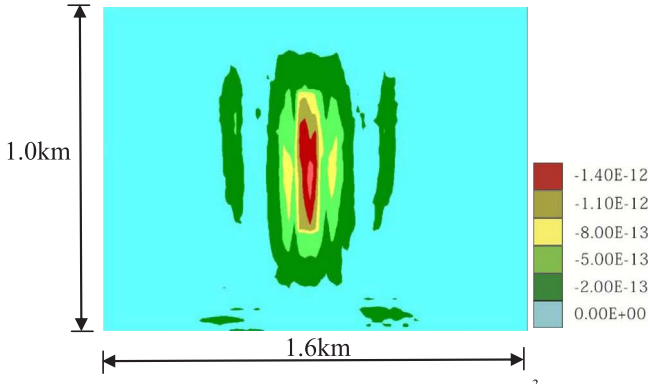

(a) The modified mineralization rate of Pb (kmol/(m^3·s))

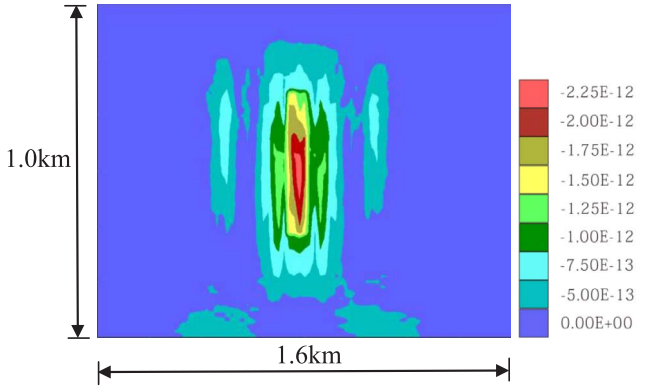

(b) The modified mineralization rate of Zn (kmol/(m^3·s))

Fig. 13. Distributions of modified mineralization rates of (a) Pb and (b) Zn.

$$\begin{aligned}
\log C^{e}_{Zn^{2+}} &= -0.001136T - 5.8239 \ (25\ ^\circ\text{C} \leqslant T < 50\ ^\circ\text{C}) \\
\log C^{e}_{Zn^{2+}} &= 0.000694T - 5.9208 \ (50\ ^\circ\text{C} \leqslant T < 100\ ^\circ\text{C}) \\
\log C^{e}_{Zn^{2+}} &= 0.00233T - 5.8861 \ (100\ ^\circ\text{C} \leqslant T < 150\ ^\circ\text{C}) \\
\log C^{e}_{Pb^{2+}} &= 0.004336T - 5.7696 \ (150\ ^\circ\text{C} \leqslant T < 200\ ^\circ\text{C}) \\
\log C^{e}_{Zn^{2+}} &= 0.003924T - 5.5528 \ (200\ ^\circ\text{C} \leqslant T < 250\ ^\circ\text{C}) \\
\log C^{e}_{Zn^{2+}} &= -0.002238T - 5.3566 \ (250\ ^\circ\text{C} \leqslant T < 300\ ^\circ\text{C}) \\
\log C^{e}_{Zn^{2+}} &= 0.000528T - 5.4686 \ (300\ ^\circ\text{C} \leqslant T < 350\ ^\circ\text{C}) \\
\log C^{e}_{Zn^{2+}} &= -0.000274T - 5.4949 \ (350\ ^\circ\text{C} \leqslant T < 400\ ^\circ\text{C})
\end{aligned} \tag{13}$$

where $C^{e}_{Zn^{2+}}$ is the equilibrium concentration of Zn^{2+} . Note that equilibrium concentration of Zn^{2+} at temperatures between 350 ℃ and 400 ℃ is extrapolated.Fig. 9 shows the behavior of Zn^{2+} in equilibrium concentration with temperature in *NaCl* buffer, and Fig. 10 shows the behavior of Zn^{2+} equilibrium concentration with pressure in the *NaCl* buffer. Similarly, Fig. 7 shows the behavior of the derivative of Zn^{2+} equilibrium concentration with temperature in *NaCl* buffer. The solid line represents experimental data, while the dotted line is extrapolated.As shown in Figs. 7–11, the experimental data obtained for Pb^{2+} and Zn^{2+} in equilibrium concentration, which were obtained under the concentration of sulfide ion (S^{2-}), are not constant. The TOUGHREACT

Table 3
Rock material parameters assigned for the actual model (Cai et al., 2002; Liu and Dai, 2014; Ju et al., 2011).

Rock types	Density (kg/m^3)	Specific heat capacity (J/kg·K)	Linear thermal expansion coefficient (10^{-6}/K)	Conductivity (W/m·K)	Fluid volumetric thermal expansion (10^{-6}/K)	Grain volumetric thermal expansion (10^{-6}/K)	Permeability (m^2)	Porosity (%)
Limestone	2460	660	6.60	3.2	620	28.1	1.00×10^{-14}	20
Quaternary	2580	790	8.40	3.4	720	31.9	2.00×10^{-11}	25
Granite	2530	710	10.80	3.0	540	25.4	1.00×10^{-14}	18
Skarn	2480	670	6.80	3.3	630	29.2	1.00×10^{-14}	21
Fault zone	2400	2200	13.90	3.0	820	41.7	1.00×10^{-10}	30

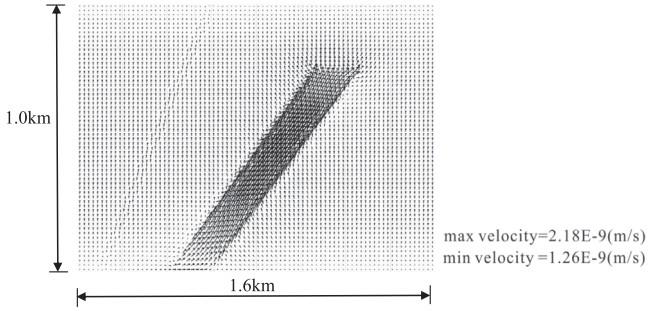

Fig. 14. Distributions of pore-fluid velocity with a unit of m/s: the maximum velocity is 2.18×10^{-9} m/s , while the minimum velocity is 1.26×10^{-9} m/s . These values take place within the fault zone.

calculated equilibrium concentrations of Pb^{2+} and Zn^{2+} at different temperatures and pressures clearly show that their equilibrium concentrations are influenced more by temperature and less pressure, as Fig. 10 shows that pressure has little effect on the equilibrium concentration of Zn^{2+}.

4. Simulation results for the Hutouya Pb-Zn deposit and discussion

Since the main E-W trending secondary fault structure was formed before mineralization occurred, the rock deformation of the intrusion was neglected. The relevant rock material parameters listed in Table 2 were used in the numerical simulation, and the simulation results of the generic model are shown below.

Fig. 12 shows the distributions of temperature and the first-order partial derivatives of temperature in *x* and *y* directions in the generic model. As mentioned by Zhao et al. (2008a, 2009), temperature localization can provide appropriate conditions for orebody formation in some regions of a hydrothermal system. On the basis of modern mineralization theory, the place with the greatest temperature change and a more rapid pore-fluid flow is more favorable for the formation of orebodies (Ord et al., 2002; Zhao et al., 2002, 2008a). Since the first-order partial derivatives of temperature in *x* and *y* directions represent the temperature gradients in each direction, we can use them to roughly estimate the best locations for orebody formation in a hydrothermal system.Fig. 13 (a) shows the modified mineralization rate of Pb, and Fig. 13 (b) shows the modified mineralization rate of Zn. Since a negative mineralization rate indicates precipitation of a mineral and a positive mineralization rate indicates that a mineral is in solution, the generic model clearly shows the regions where galena and sphalerite are precipitated. The modeling results show that the greatest precipitation of Pb-Zn ore occurs in the region between 100 and 300 °C (Lei, 2014). Since the pressure dependence of solubility is typically weak and usually neglected in the chemical reaction of galena and sphalerite (Pauling, 1988), the pressure changes have not been coded in the program (Liu and Dai, 2014). Because the experimental data for the equilibrium concentrations of Pb^{2+} and Zn^{2+} provided by the TOUGHREACT code showed that pore-fluid pressure has little impact

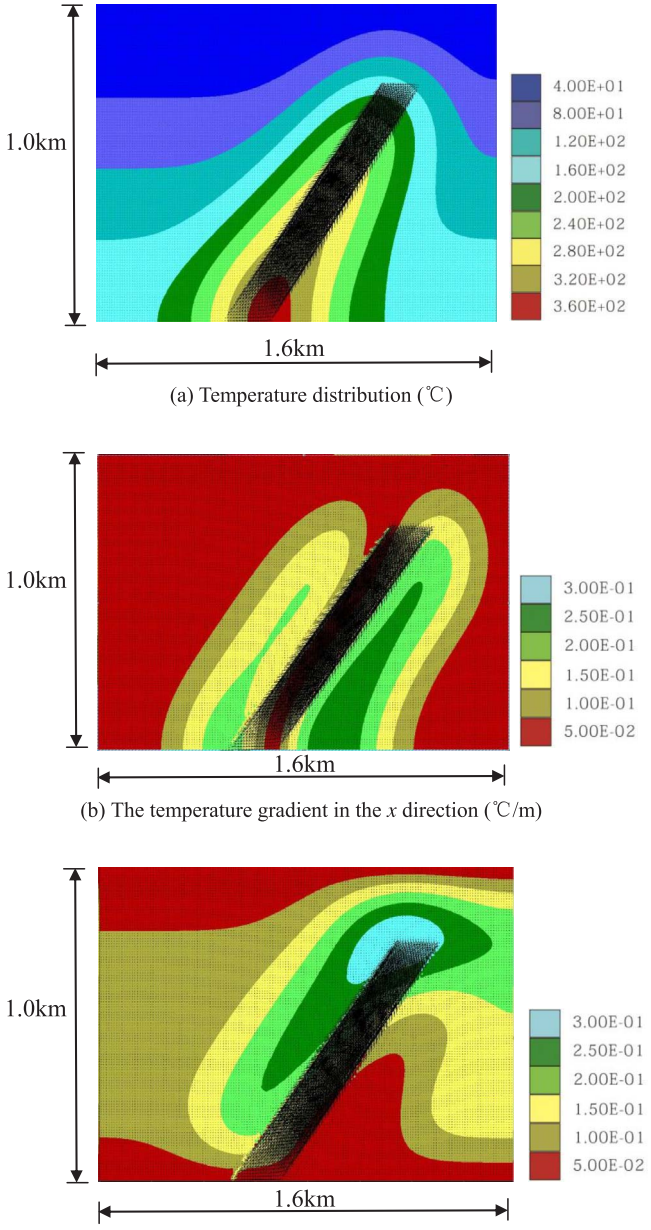

Fig. 15. Distributions of (a) temperature, (b) temperature gradient in *x* direction and (c) temperature gradient in *y* direction.

on the equilibrium of the chemical reaction of galena and sphalerite in the Hutouya ore district, the effect of pore-fluid pressure on the precipitation of galena and sphalerite has not been considered in the associated numerical simulations.

The simulation results of the geological conceptual model are shown

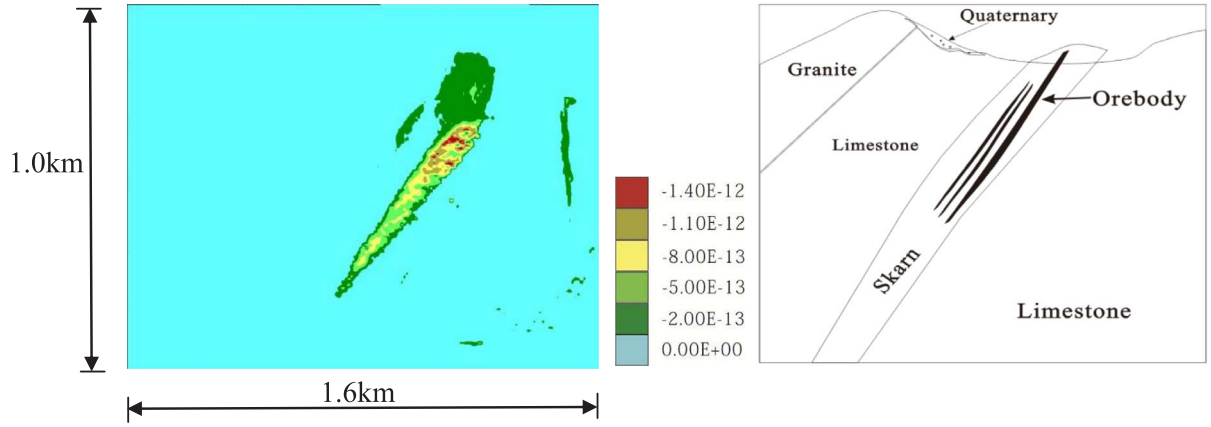

(a) The modified mineralization rate of Pb (kmol/(m^3·s))

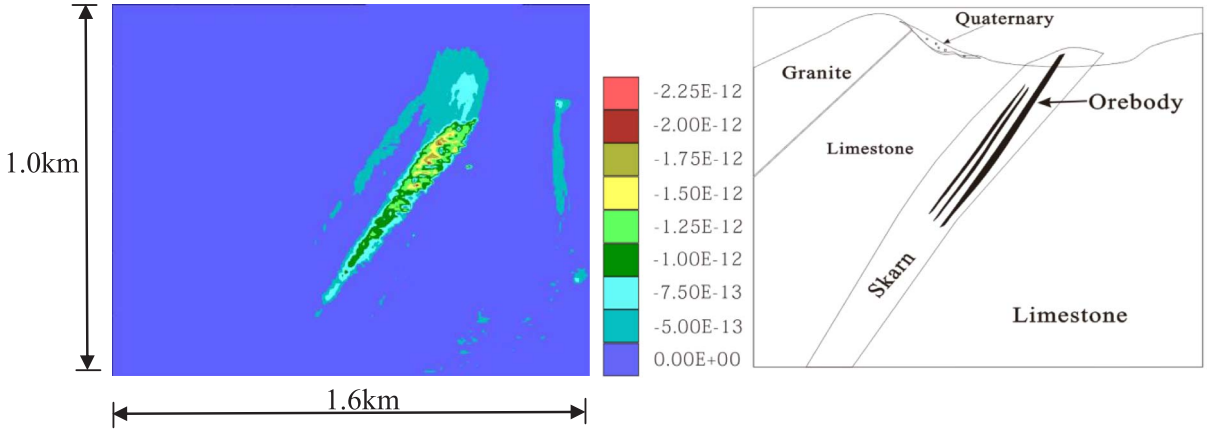

(b) The modified mineralization rate of Zn (kmol/(m^3·s))

Fig. 16. Distributions of the modified mineralization rates of (a) Pb and (b) Zn.

below. Note that the relevant rock material parameters listed in Table 3 were used in the numerical modeling while neglecting rock deformation.

Fig. 14 shows the distribution of pore-fluid velocity, and Fig. 15 shows the distributions of temperature and temperature gradients in x and y directions of the actual model. The results in Fig. 12 show that the temperature distribution is almost completely symmetrical along the fault trend direction. Fig. 15 shows that the temperature distribution diffuses along the fault trend with a dip angle of 65° to the east, near the west at the bottom. The temperature gradients in x and y directions shows that the greatest temperature variation occurs in the regions that are favorable for galena and sphalerite precipitation, which indicate that both the position and intrusion direction of the fault zone had a significant effect on the temperature localization in this hydrothermal system. A calculation of the Peclet number of the hydrothermal system in the Hutouya Pb-Zn ore district is also interesting. Based on the pore-fluid velocity results (shown in Fig. 14) and the physical parameters used in the numerical model, the Peclet number of the simulated hydrothermal system is approximately 3.1, indicating that advective heat transfer predominates in the simulated hydrothermal system.

Fig. 16 shows the distributions of the modified mineralization rates of Pb and Zn in the realistic model of the Hutouya Pb-Zn deposit. Fig.16(a) shows the modified galena mineralization rate, and Fig.16(b) shows the modified sphalerite mineralization rate. Since the modified mineralization rate is dependent on the specific mineral, it can be used to predict the exact amount of ore precipitated, if the mineralization time is known. However, if the grade of precipitated ore is known, we can estimate the mineralization time with the following formulas:

$$t_{m(k)}(s) = \frac{\overline{W_k} \times \rho_k}{MR_k \times Q_k} \quad \text{(with a unit of seconds)} \tag{14}$$

$$t_{(year)} = 365 \times 24 \times 3600\ (s) \tag{15}$$

$$MP_k = \frac{t_{m(k)}}{t_{(year)}} \quad \text{(with a unit of years)} \tag{16}$$

where $\overline{W_k}$ is the grade of a mineral k (k = Pb or Zn), ρ_k is density of the rock containing a mineral k (k = Pb or Zn) with units of kilogram per cubic meter, MR_k is the modified mineralization rate of a mineral k (k = Pb or Zn), Q_k is atomic weight of a mineral k (k = Pb or Zn), $t_{m(k)}$ is duration of the metallogenic process of a mineral k (k = Pb or Zn) with unit of seconds, $t_{(year)}$ is number of seconds in a year, MP_k is duration of the metallogenic process of a mineral k (k = Pb or Zn). We know that the average grades of Pb and Zn in the Hutouya Pb-Zn deposit are, respectively, 3.26% and 4.34%, so we can estimate that the duration of metallogenic process for galena in the Hutouya Pb-Zn deposit is between 10,000 and 60,000 years and that the duration of metallogenic process for sphalerite is between 30,000 and 100,000 years.

5. Conclusions

The Hutouya Pb-Zn deposit is a typical hydrothermal deposit in the

Qinghai province of China. An application of mineralization rate theory to two examples of the Hutouya mineralizing systems using numerical simulation has demonstrated the following:

(1) Hydrothermal fluid flow is a key controlling factor of mineralization in the Hutouya Pb-Zn deposit as clearly implied by Fig. 16, which shows that the simulated metallogenic location matches the field geological exploration results.
(2) The numerical results indicate that the metallogenic temperature of galena in the Hutouya Pb-Zn deposit is between 100 and 250 °C, and that of sphalerite is between 150 and 300 °C. The metallogenic temperature range provided by the TOUGHREACT code for the Hutouya Pb-Zn deposit is consistent with that derived from a geological interpretation (Lei et al., 2014b; Xu, 2010). Figs. 7 and 9 show that the most favorable metallogenic temperatures of galena and sphalerite are 150 and 250 °C, respectively.
(3) The duration of mineralization process for galena and sphalerite in the Hutouya Pb-Zn deposit are approximately 10,000 to 60,000 years and 30,000 to 100,000 years, respectively. Galena and sphalerite mineralization corresponds to the quartz sulfide stage and the ore-forming period of galena was later than that of the sphalerite. These results are consistent with previous research (Lei et al., 2014b).

Acknowledgements

This study was funded by the Natural Science Foundation of China (Grant No: 41472302) and the National Key Research and Development Program of China (Grant No: 2017YFC0601503). We thank the anonymous referees for their valuable comments, which led to the significant improvement of an earlier version of this paper.

References

Alt-Epping, P., Zhao, B.C., 2010. Reactive mass transport modeling of a three-dimensional vertical fault zone with a finger-like convective flow regime. J. Geochem. Explor. 106, 8–23.
Cai, M., Zhan, M., Peng, S., Meng, X., Liu, G., 2002. Study of mesozoic metallogenic geological setting and dynamic mechanism in Yunkai Area. Miner. Deposits 21, 264–269 (in Chinese with English abstract).
Cundall, P.A., Board, M., 1988. A microcomputer program for modelling large-strain plasticity problems. In: Swoboda, C. (Ed.), Numerical Methods in Geomechanics: Proceedings, 6th International Conference on Numerical Methods in Geomechanics. Balkema, Rotterdam, pp. 2101–2108.
Gao, Y., Li, W., Li, K., Qian, B., Zhang, Z., He, S., Liu, Y., Zhang, J., Wang, Y., Zang, Y., 2013. Fluid inclusions, isotoopic geochemistry and genesis of the Hutouya Zn-Pb deposit in Qimantage, Qinghai province. Geol. Bull. China 32, 1631–1642 (in Chinese with English abstract).
Gao, X., Zhang, D., Absai, V., Feng, H., Yi, J., 2015. Computational simulation of coupled geodynamics for forming the Makeng deposit in Fujian Province, China: constraints of mechanics, thermotics and hydrology. J. Geochem. Explor. 160, 31–43.
Garven, G., Gee, S., Person, M.A., Sverjensky, D.A., 1993. Genesis of stratabound ore deposits in the midcontinent basins of North America. 1. The role of regional groundwater flow. Am. J. Sci. 293 497-497.
Gessner, K., Kühn, M., Rath, V., Kosack, C., Blumenthal, M., Clauserss, C., 2009. Coupled process models as a tool for analysing hydrothermal systems. Surv. Geophys. 30, 133–162.
Gow, P., Upton, P., Hill, K., 2002. Copper-Gold mineralization in the New Guinea: numerical modeling of collision, fluid flow and intrusion-related hydrothermal system. Aust. J. Earth Sci. 49, 753–771.
He, H., Liu, W., Yang, X., Luo, Y., Fan, Y., 2014. Mineral resource predication and evaluation based on uncertainty measure theory: a case of Hutouya min field of Qinghai. J. Northwest Univ. (Nat. Sci. Ed.) 44, 615–620 (in Chinese with English abstract).
Hobbs, B.E., Zhang, Y., Ord, A., 2000. Application of coupled deformation, fluid flow, thermal and chemical modeling to predictive mineral exploration. J. Geochem. Explor. 69, 505–509.
Hobbs, B.E., Ord, A., Peng, S., Mühlhaus, H.B., Liu, L., 2004. Theoretical investigation of convective instability in inclined and fluid-saturated three-dimensional fault zones. Tectonophysics 387, 47–64.
Hobbs, B.E., Ord, A., Kühn, M., Mühlhaus, H.B., Peng, S., 2006. Numerical simulation of double-diffusion driven convective flow and rock alteration in three-dimensional fluid-saturated geological fault zones. Comput. Methods Appl. Mech. Eng. 195, 2816–2840.
Hobbs, B.E., Ord, A., Hornby, P., Peng, S., Liu, L., 2007. Mineral precipitation associated with vertical fault zones: the interaction of solute advection, diffusion and chemical kinetics. Geofluids 7, 3–18.
Hobbs, B.E., Ord, A., Hornby, P., Peng, S., 2008. Effect of reactive surface areas associated with different particle shapes on chemical-dissolution front instability in fluid-saturated porous rocks. Transp. Porous Media 73, 75–94.
Hobbs, B.E., Ord, A., Peng, S., 2010a. Effects of mineral dissolution ratios on chemical-dissolution front instability in fluid-saturated porous rocks. Transp. Porous Media 82, 317–335.
Hobbs, B.E., Ord, A., Zhao, B.C., 2010b. Theoretical analyses of the effects of solute dispersion on chemical-dissolution front instability in fluid-saturated porous rocks. Transp. Porous Media 84, 629–653.
Hobbs, B.E., Regenauer-Lieb, K., Ord, A., 2011. Computational simulation for the morphological evolution of nonaqueous-phase-liquid dissolution fronts in two-dimensional fluid-saturated porous media. Comput. Geosci. 15, 167–183.
Hobbs, B.E., Ord, A., Zhao, B.C., 2017. Why asymptotic limit of the acid dissolution capacity can lead to a sharp dissolution front in chemical dissolution of porous rocks? Int. J. Numer. Anal. Meth. Geomech. http://dx.doi.org/10.1002/nag.2690.
Hornby, P., Ord, A., Peng, S., 2006a. Numerical modelling of fluids mixing, heat transfer and non-equilibrium redox chemical reactions in fluid-saturated porous rocks. Int. J. Numer. Meth. Eng. 66, 1061–1078.
Hornby, P., Peng, S., Liu, L., 2006b. Theoretical and numerical analyses of pore-fluid flow patterns around and within inclined large cracks and faults. Geophys. J. Int. 166, 970–988.
Hornby, P., Ord, A., Peng, S., Liu, L., 2008. Theoretical and numerical analyses of chemical-dissolution front instability in fluid-saturated porous rocks. Int. J. Numer. Anal. Meth. Geomech. 32, 1107–1130.
Itasca Consulting Group, 2012. FLAC User's Guide. Itasca Consulting Group Inc, Minneapolis.
Ju, M., Zhao, B.C., Dai, T., Yang, J., 2011. Finite element modeling of pore-fluid flow in the Dachang ore district, Guangxi, China: implications for hydrothermal mineralization. Geosci. Front. 2 (3), 463–474.
Lai, J., Huang, M., Wang, X., Song, W., Lei, Y., Kong, D., 2015. Study on mineralization of typical polymetallic deposits of Qimantage metallogenic in Qinghai province. Central South University Press, Changsha (in Chinese).
Lei, Y., 2013. Geological and geochemical characteristics, metallogenesis of Hutouya deposit, Qinghai province. Master thesis of Central South University (in Chinese with English abstract).
Lei, H., 2014. Typomorphic studies of sphalerite in the Hutouya Pb-Zn deposit from Qinghai. Master thesis of Central South University (in Chinese with English abstract).
Lei, X., Chen, Y., Zhao, J., 2013. Three-dimensional thermo-mechanical modeling of the Cenozoic uplift of the Tianshan mountains driven tectonically by the Pamir and Tarim. J. Asian Earth Sci. 62, 797–811.
Lei, H., Wang, Z., Lu, A., Gu, X., Yi, L., 2014a. A typomorphic study of sphalerite from the Hutouya Pb-Zn deposit in Qinghai province. Acta Petrol. Mineral. 33, 924–936 (in Chinese with English abstract).
Lei, Y., Lai, J., Wang, X., Su, S., Wang, S., Tao, S., 2014b. Origin and evolution of ore-forming material of Hutouya polymetallic deposit. Chin. J. Nonferrous Metal 24 (8), 2117–2128 (in Chinese with English abstract).
Li, H., Xi, X., 2012. Geochemistry and sedimentary exhalative mineralization in Hutouya-Kendekeke field, Qinghai Province, China. Chin. J. Nonferrous Metal 22, 772–783 (in Chinese with English abstract).
Li, H., Liu, H., Chen, Y., Liu, T., 2003. The metallogenic environments analysis and prospecting idea of the Pb-Zn deposit in Jiuyishan-Guposhan area. Contribut. Geol. Miner. Resour. Res. 18 (1), 13–20 (in Chinese with English abstract).
Lin, G., Hobbs, B.E., Ord, A., Mühlhaus, H.B., 2003. Theoretical and numerical analyses of convective instability in porous media with temperature-dependent viscosity. Commun. Numer. Methods Eng. 19, 787–799.
Lin, G., Zhou, Y., Wei, X., 2006. Structure controls on fluid flow and related mineralization in the Xiangshan uranium deposit, Southern China. J. Geochem. Explor. 89, 231–234.
Lin, G., Hobbs, B.E., Zhang, L., Zhou, Y., 2008. Potential effects of upward throughflow on thermal structure models within the continental lithospheric mantle-crust. Chin. J. Geophys. 51 (2), 393–401.
Lin, G., Peng, M., Zhang, L., Zhang, D., Liu, S., 2009. Numerical analysis and simulation experiment of lithospheric thermal structures in the South China Sea and the Western Pacific. J. Earth Sci. 20, 85–94.
Liu, Y., Dai, T., 2014. Numerical modeling of pore-fluid flow and heat transfer in the Fushan iron ore district, Hebei, China: implications for hydrothermal mineralization. J. Geochem. Explor. 144, 115–127.
Liu, Y., Dai, T., 2015. Computational simulation of iron ore-forming processes in the Caiyuanzi siderite ore district, Guizhou, China. J. Geochem. Explor. 1158, 155–167.
Liu, Y., Cao, L., Li, Z., 1984. Element geochemistry. Science press, Beijing (in Chinese).
Liu, L., Yang, G., Peng, S., 2005. Numerical modelling of coupled geodynamical processes and its role in facilitating predictive ore discovery: an example from Tongling, China. Resour. Geol. 55, 21–31.
Liu, Y., Mo, X., Zhang, X., Xu, G., 2006. The geochemical characteristics and the meaning of skarn- type deposits in Yemanquan area, Eastern Kunlun. Geol. Miner. Resour. South China 3, 31–36 (in Chinese with English abstract).
Liu, L., Zhao, Y., Zhao, B.C., 2010a. Coupled geodynamics in the formation of Cu skarn deposit in Tongling-Anqing district, China: computational modeling and implications for exploration. J. Geochem. Explor. 106, 146–155.
Liu, L., Zhou, R., Zhao, B.C., 2010b. Constraints of tectonic stress regime on mineraliazation system related to the hypabyssal intrusion: implication from the computational modeling experiments on the geodynamics during cooling process of the Yuenshan intrusion in Anqing district, China. Acta Petrol. Sin. 26, 2869–2878 (in Chinese with English Abstract).
Liu, L., Wan, C., Zhao, Y., 2011. Geodynamic constraints on orebody localization in the

Anqing orefield, China: computational modeling and facilitating predictive exploration of deep deposits. Ore Geol. Rev. 43, 249–263.
Lu, H., 1975. The formation temperature of sphalerite measured by geologic thermometer and barometer. Earth Environ. 2, 34–47 (in Chinese).
Luo, Y., 2014. The analysis of Ore-controlling structure and target section forecast of the VII ore in Qinghai Qimanntage Hutouya orefield. Master Thesis of Chang'an University (in Chinese with English abstract).
Ma, S., Feng, C., Li, G., Shu, X., 2012. Sulfur and lead isotope compositions of the Hutouya copper-lead-zinc polymetallic deposit in Qinghai province and their genetic significance. Geol. Explor. 48, 321–331 (in Chinese with English abstract).
Ma, S., Feng, C., Zhang, D., Li, D., Shu, X., Liu, J., Du, S., 2013. Alteration and mineralization zoning of Hutouya polymetallic deposit in Qimantage area, Qinghai province. Miner. Deposits 32, 109–121 (in Chinese with English abstract).
McLellan, J.D., Oliver, N.H.S., Schaubs, P.M., 2004. Fluid flow in extensional environments; Numerical modelling with an application to Hamersley iron ores. J. Struct. Geol. 26, 1157–1171.
McLellan, J.D., Oliver, N.H.S., Hobbs, B.E., Rowland, J.V., 2009. Convection stability in the Taupo Volcanic Zone, New Zealand. J. Geochem. Explor. 101, 69.
McLellan, J.D., Oliver, N.H.S., Hobbs, B.E., Rowland, J.V., 2010. Modelling fluid convection stability in continental faulted rifts with applications to the Taupo Volcanic Zone, New Zealand. J. Volcanol. Geoth. Res. 190, 109–122.
Mclellan, J.G., O'Sullivan, R., Miller, B., Taylor, D., 2014. Geomechanical Modelling of the Mount Isa Copper Deposit-Predicting Mineralisation. International Mining Geology Conference.
Mclellan, J.G., Conn, J., Howe, D., Gates, K., 2014. Structural Controls and Strain Partitioning in the Red October Gold Mine, Western Australia. International Mining Geology Conference.
Oliver, N.H.S., McLellan, J.G., Hobbs, B.E., Cleverley, J.S., Ord, A., Feltrin, L., 2006. Numerical models of deformation, heat transfer and fluid flow across basement-cover interfaces during basin-related mineralization, with application to the Mt Isa Pb-Zn district. Economic Geology 100th Anniversary Volume 101, 1–31.
Ord, A., Hobbs, B.E., Zhang, Y., Broadbent, G.C., Brown, M., Willetts, G., Sorjonen-Ward, P., Walshe, J., 2002. Geodynamic modeling of the Century deposit, Mt Isa Province, Queensland. Aust. J. Earth Sci. 49, 1011–1039.
Ord, A., Hornby, P., Peng, S., 2008a. Morphological evolution of three-dimensional chemical dissolution front in fluid-saturated porous media: a numerical simulation approach. Geofluids 8, 113–127.
Ord, A., Peng, S., Liu, L., 2008b. Inversely-mapped analytical solutions for flow patterns around and within inclined elliptic inclusions in fluid-saturated rocks. Math. Geosci. 40, 179–197.
Ord, A., Hobbs, E.B., Zhao, B.C., 2010. Theoretical and numerical investigation into roles of geofluid flow in ore forming systems: integrated mass conservation and generic model approach. J. Geochem. Explor. 106, 251–260.
Ord, A., Hobbs, E.B., Zhao, B.C., 2012. Effects of domain shapes on the morphological evolution of nonaqueous-phase-liquid dissolution fronts in fluid-saturated porous media. J. Contam. Hydrol. 138–139, 123–140.
Ord, A., Hobbs, E.B., Zhao, B.C., 2013a. Analytical solutions of nonaqueous-phase-liquid dissolution problems associated with radial flow in fluid-saturated porous media. J. Hydrol. 494, 96–106.
Ord, A., Hobbs, E.B., Zhao, B.C., 2013b. Effects of medium permeability anisotropy on chemical-dissolution front instability in fluid-saturated porous rocks. Transp. Porous Media 99, 119–143.
Ord, A., Hobbs, E.B., Zhao, B.C., 2016. Chemical dissolution-front instability associated with water-rock reactions in groundwater hydrology: analyses of porosity-permeability relationship effects. J. Hydrol. 540, 1078–1087.
Ord, A., Hobbs, E.B., Zhao, B.C., 2017. Effects of acid dissolution capacity on the propagation of an acid-dissolution front in carbonate rocks. Comput. Geosci. 102, 109–115.
Pauling, L., 1988. General Chemistry. Dover Publications Inc., New York.
Peng, S., Ord, A., Hobbs, B.E., Zhao, B.C., 2008. Particle simulation of spontaneous crack generation associated with the laccolithic type of magma intrusion processes. Int. J. Numer. Meth. Eng. 75, 1172–1193.
Peng, S., Liu, L., Ord, A., 2011. Computational simulation of convective flow in the Earth's crust with consideration of dynamic crust-mantle interactions. J. Central South Univ. Technol. 18, 2080–2084.
Phillips, O.M., 1991. Flow and Reactions in Permeable Rocks. Cambridge University Press, Cambridge.
Potma, W., Roberts, P.A., Schaubs, P.M., Sheldon, H.A., Zhang, Y., Hobbs, B.E., Ord, A., 2008. Predictive targeting in Australian orogenic-gold systems at the deposit to district scale using numerical modelling. Aust. J. Earth Sci. 55 (1), 101–122.
Poulet, T., Regenauer-Lieb, K., 2015a. Numerical modeling of toxic nonaqueous-phase-liquid removal from contaminated groundwater systems: mesh effect and discretization error estimation. Int. J. Numer. Anal. Meth. Geomech. 39, 571–593.
Poulet, T., Regenauer-Lieb, K., 2015b. Replacement of annular domain with trapezoidal domain in computational modeling of nonaqueous-phase-liquid dissolution-front propagation problems. J. Central South Univ. 22, 1841–1846.
Poulet, T., Regenauer-Lieb, K., Hobbs, B.E., 2013. Computational modeling of moving interfaces between fluid and porous medium domains. Comput. Geosci. 17, 151–166.
Qu, H., Feng, C., Pei, R., He, S., Liu, J., Wang, H., Zhou, J., 2015. Thermochronology of Hutouya skarn-type copper-lead-zinc polymetallic ore district in the Qimantage area, Qinghai province. Acta Geol. Sinica 89, 498–509 (in Chinese with English abstract).
Reid, L.B., Regenauer-Lieb, K., Poulet, T., 2012a. A porosity-gradient replacement approach for computational simulation of chemical-dissolution front propagation in fluid-saturated porous media including pore-fluid compressibility. Comput. Geosci. 16, 735–755.
Reid, L.B., Regenauer-Lieb, K., Zhao, B.C., 2012b. Some fundamental issues in computational hydrodynamics of mineralization. J. Geochem. Explor. 112, 21–34.
Schaubs, P., Zhao, B.C., 2002. Numerical modelling of gold-deposit formation in the Bendigo-Ballarat zone, Victoria. Aust. J. Earth Sci. 49, 1077–1096.
Schaubs, P., Hobbs, B., Zhao, B.C., 2016a. Computational simulation of seepage instability problems in fluid-saturated porous rocks: potential dynamic mechanisms for controlling mineralization patterns. Ore Geol. Rev. 79, 180–188.
Schaubs, P., Hobbs, B., Zhao, B.C., 2016b. Acquisition of spatially-distributed geochemical data in geoinformatics: computational simulation approach. J. Geochem. Explor. 164, 18–27.
Schaubs, P., Hobbs, B., Zhao, B.C., 2017. Effects of porosity heterogeneity on chemical dissolution-front instability in fluid-saturated rocks. J. Central South Univ. 24, 720–725.
Schmidt Mumm, A., Brugger, J., Schacht, U., 2010. Fluids in geological processes: the present state and future outlook. J. Geochem. Explor. 106, 1–7.
Shu, X., Wang, X., Zhang, Y., Zhu, W., 2012. Determination of multifarious genesis and prospecting of polymetallic deposit in Hutouya, Qinghai. Northwestern Geol. 45, 165–173 (in Chinese with English abstract).
Song, Z., Jia, Q., Zhang, Z., 2010. Study on geological feature and origin of Yemaquan Fe-Cu deposit in Qimantage area, Easter Kunlun. Northwestern Geol. 43, 209–217 (in Chinese with English abstract).
Sorjonen-Ward, P., Zhang, Y., 2002. Numerical modelling of orogenic processes and mineralization in the south eastern part of the Yilgarn Craton, Western Australia. Aust. J. Earth Sci. 49, 935–964.
Tiziana, A., Claudia, C., Andrea, M., Alessandro, T., 2013. Understanding Etna flank instability through numerical models. J. Volcanol. Geoth. Res. 251, 112–126.
Walshe, J.L., Mühlhaus, H.B., Ord, A., 2001. Finite element modelling of fluid-rock interaction problems in pore-fluid saturated hydrothermal/sedimentary basins. Comput. Methods Appl. Mech. Eng. 190, 2277–2293.
Xiao, H., He, X., Feng, T., Wang, E., 2005. Research on coupling laws between EME and stress fields during deformation and fracture of mine tunnel excavation based on FLAC2D. Chin. J. Rock Mech. Eng. 24, 2304–2309 (in Chinese with English abstract).
Xing, H.L., Makinouchi, A., 2008. Three-dimensional finite element simulation of large-scale nonlinear contact friction problems in deformable rocks. J. Geophys. Eng. 5, 27–36.
Xu, G., 2010. Study of deposit geochemistry in the Qimantage polymetallic metallogenic belt, Qinghai province. PhD Thesis of Kunming University of Science and Technology (in Chinese with English abstract).
Xu, T., Sonnenthal, E., Spycher, N., Pruess, K., 2004. TOUGHREACT user's guide: a simulation program for nonisothermal multiphase reactive geochemical transport in variably saturated geologic media. Earth Sciences Division, Lawrence Berkeley National Laboratory Report CA 94720, Berkeley, California.
Yan, Y., Lin, G., Wang, Y.J., Guo, F., 2003. Apatite fission track age of Mesozoic sandstones from Beipiao basin, eastern China: implications for basin provenance and tectonic evolution. Geochem. J. 37, 377–389.
Yang, J.W., Feng, Z., Luo, X., Chen, Y., 2010. Three-dimensional numerical modeling of salinity variations in driving basin-scale ore-forming fluid flow: example from Mount Isa Basin, northern Australia. J. Geochem. Explor. 106, 236–243.
Yang, X., Liu, W., He, H., Qu, C., Zhao, H., Jiang, W., Fan, Y., Yu, H., 2015. The geology and prospecting of Jingren-Hutouya orefield in Qimantage of Qinghai province: type of magma-thermodynamic structure and structure-lithofacies geological mapping. Earth Sci. Front. 22, 105–112 (in Chinese with English abstract).
Yao, L., Lv, Z., Yu, X., Pang, Z., Cai, Y., Liu, P., Liu, C., Wang, F., 2015. Petrogenesis, geochemistry and zircon U-Pb Age of the granite from No. VII section of Hutouya deposit, Qimantage area, Qinghai province, and its geological significance. J. Jilin Univ. (Earth Sci. Ed.) 45, 743–758 (in Chinese with English abstract).
Zhang, Y., Barnicoat, A., Lin, G., 2003. The influence of faulting on host-rock permeability, fluid flow and ore genesis of gold deposits: a theoretical 2D numerical model. J. Geochem. Explor. 78–79, 279–284.
Zhang, Y., Schaubs, P.M., Barnicoat, A., 2008. Fault-related dilation, permeability enhancement, fluid flow and mineral precipitation patterns: numerical models, in: Wibberley, C.A.J., Kurz, W., Imber, J., Holdsworth, R.E., Collettini, C. (Eds.), The Internal Structure of Fault Zones: Implications for Mechanical and Fluid-flow Properties. Geological Society 299. Special Publications, London, 239–255.
Zhang, L., Li, Z., Lin, G., Guo, H., 2011. Numerical simulation of effects of upward throughflow on thermal structure and the thickness of the continental lithosphere. J. Geophys. Eng. 8, 322–329.
Zhang, A., Liu, G., Feng, C., Mo, X., Yang, L., Liu, Y., He, S., Ma, Y., 2013. Geochemical characteristics and ore-controlling factors of Hutouya polymetallic deposit, Qinghai province. Miner. Deposits 32, 94–108 (in Chinese with English abstract).
Zhao, C., 2009. Dynamic and Transient Infinite Elements: Theory and Geophysical, Geotechnical and Geoenvironmental Applications. Springer, Berlin.
Zhao, C., 2014. Physical and Chemical dissolution Front Instability in Porous Media: Theoretical Analyses and Computational Simulations. Springer, Berlin.
Zhao, C., 2015. Advances in numerical algorithms and methods in computational geosciences with modeling characteristics of multiple physical and chemical processes. Sci. China Technol. Sci. 58, 783–795.
Zhao, C., 2016. Computational methods for simulating some typical problems in computational geosciences. Int. J. Comput. Methods 13, 1–17.
Zhao, C., Hobbs, B.E., Mühlhaus, H.B., 1998. Finite element modelling of temperature gradient driven rock alteration and mineralization in porous rock masses. Comput. Methods Appl. Mech. Eng. 165, 175–187.
Zhao, C., Lin, G., Wang, Y., Mühlhaus, H.B., Ord, A., 2002. Finite element modeling of reactive fluids mixing and mineralization in pore-fluid saturated hydrothermal/sedimentary basins. Eng. Comput. 19, 364–385.
Zhao, C., Hobbs, B.E., Ord, A., 2008a. Convective and Advective Heat Transfer in Geological Systems. Springer, Berlin.

Zhao, C., Hobbs, B.E., Ord, A., 2008b. Investigating dynamic mechanisms of geological phenomena using methodology of computational geosciences: an example of equal-distant mineralization in a fault. Sci. China, Ser. D Earth Sci. 51, 947–954.
Zhao, C., Hobbs, B.E., Ord, A., 2009. Fundamentals of Computational Geoscience: Numerical Methods and Algorithms. Springer, Berlin.
Zhao, C., Hobbs, B.E., Ord, A., 2010. Theoretical analyses of nonaqueous-phase-liquid dissolution induced instability in two-dimensional fluid-saturated porous media. Int. J. Numer. Anal. Meth. Geomech. 34, 1767–1796.
Zhao, C., Hobbs, B.E., Ord, A., 2012a. Effects of medium and pore-fluid compressibility on chemical-dissolution front instability in fluid-saturated porous media. Int. J. Numer. Anal. Methods Geomech. 36, 1077–1100.
Zhao, C., Reid, L.B., Regenauer-Lieb, K., 2012b. Some fundamental issues in computational hydrodynamics of mineralization: a review. J. Geochem. Explor. 112, 21–34.
Zhao, C., Hobbs, B.E., Ord, A., 2013. Theoretical analyses of acidization-dissolution front instability in fluid-saturated carbonate rocks. Int. J. Numer. Anal. Meth. Geomech. 37, 2084–2105.
Zhao, C., Hobbs, B.E., Alt-Epping, P., 2014. Modelling of ore-forming and geoenvironmental systems: roles of fluid flow and chemical reaction processes. J. Geochem. Explor. 144, 3–11.
Zhao, C., Hobbs, B.E., Ord, A., 2015a. Theoretical analyses of chemical dissolution-front instability in fluid-saturated porous media under non-isothermal conditions. Int. J. Numer. Anal. Meth. Geomech. 39, 799–820.
Zhao, C., Hobbs, B.E., Ord, A., 2015b. Computational simulation of chemical dissolution-front instability in fluid-saturated porous media under non-isothermal conditions. Int. J. Numer. Meth. Eng. 102, 135–156.
Zhao, C., Hobbs, B.E., Ord, A., 2017. A new alternative approach for investigating acidization dissolution front propagation in fluid-saturated rocks. Sci. China Technol. Sci. 60, 1–14.

Further reading

Tang, H., Li, Z., 2012. Research of ore mental solubility and technology of testing. Geol. Sci. Technol. Inf. 31 (1), 137–142 (in Chinese with English abstract).
Zhang, P., Shi, F., Zhang, J., Xu, G., Yang, Z., 2012. Metallogenic sub-belt division and prospect analysis of Qimantage area, Qinghai province. Miner. Resour. Geol. 26, 265–270 (in Chinese with English abstract).